A new seismic-based strain energy methodology for coal burst forecasting in underground coal mines

Wu Cai[a,b,*], Linming Dou[a,**], Guangyao Si[c,***], Anye Cao[a], Siyuan Gong[a], Guifeng Wang[a], Shasha Yuan[a]

[a] State Key Laboratory of Coal Resources and Safe Mining, School of Mines, China University of Mining and Technology, Xuzhou, Jiangsu, 221116, China
[b] Department of Earth Science and Engineering, Royal School of Mines, Imperial College, London, SW7 2AZ, United Kingdom
[c] School of Minerals and Energy Resources Engineering, University of New South Wales, Sydney, NSW, 2052, Australia

A B S T R A C T

Coal burst has become a common safety issue in underground coal mines and its triggering mechanism is believed to be highly associated with coal state parameters including stress, strain and energy. As a powerful tool for coal burst forecasting, microseismic (MS) monitoring has the capability of directly monitoring energy release and indirectly capturing stress and strain changes. In this paper, the strain energy transfer in the process of coal burst during underground coal mining was investigated, which revealed that coal burst is caused by strain energy released from the surrounding rock, plus the additional energy input provided by the superposition of static and dynamic stresses. The seismic energy, derived from the strain energy transfer process, was defined and simulated in numerical models. Based on the modelling results, a damage mechanics model was developed to correlate stress, strain, damage and seismic energy release. In this context, a new index named as 'bursting strain energy (BSE)' was proposed to quantitatively assess coal burst propensity. This BSE index was first calibrated via numerical modelling and then successfully applied to a Chinese coal mine for coal burst forecasting. Results showed that the BSE index can effectively assess the likelihood of coal burst occurrence in the temporal domain and assess high risk regions in the spatial domain. Such practices can be conducted on a daily basis, which will contribute to the improvement of mine safety and productivity.

1. Introduction

Coal burst is currently considered as one of the most severe threats to underground safety in coal mining. It is caused by elastic strain energy released in a sudden, rapid, and violent manner from coal or coal measure rocks. A coal burst event can be accompanied by an airblast or windblast, which may disrupt mine ventilation, throw out equipment and fragmented rock blocks, release strata gas and propagate explosive dust into the air.[1,2] With the increasing depth of underground coal mining, coal extraction is facing ever-increasing stress conditions with acute occurrence and frequency of coal burst incidents. As the occurrence of coal burst is rather complex and abrupt in time and location, understanding its triggering mechanism and quantitative spatial-temporal forecasting and prevention are very challenging tasks for the improvement of mine safety and productivity.

Over last 40 years, various hypotheses for coal burst mechanism have been proposed and widely accepted by mining practitioners, from the perspectives of strength,[3] energy,[4–6] stiffness,[7–9] stability,[1,10] burst liability,[11–13] and the superposition of dynamic and static stresses.[14–16] There are three physical parameters mainly considered in these hypotheses: stress, strain, and energy. To further understand the intrinsic links between these three parameters, numerous methods for coal burst monitoring and forecasting have been reported from the viewpoint of directly or indirectly capturing stress/strain/energy responses to underground mining, such as the field measurement of microseismicity,[17–21] electromagnetic emission,[22] acoustic emission (AE),[23] coal drill cuttings,[2] and relative borehole stress.[24,25] In practice, microseismic (MS) monitoring has been recognised as the most convenient and effective method due to its very nature of real-time remote access, large monitoring scope, relatively low noise disturbance, and non-

interruption on production.

MS emissions during rock failure process is a well-documented phenomenon, which can be observed in various scales ranging from laboratory rock tests, underground mining activities, to even crustal earthquakes.[26–28] Since coal burst is highly related with coal failure processes, the emission of seismic waves can be detected via careful design monitoring arrays during underground mining operations, which may provide input for the prediction of a coal burst incident, essentially a large seismic event.

Research on the MS effects of coal/rock fracturing and mining-associated coal burst events has been carried out fruitfully over the last two decades. For instance, Friedel et al.,[29] Luxbacher et al.,[30] Luo et al.,[31] Cai et al.,[32,33] and Gong et al.[34] investigated the applications of seismic velocity tomograms in underground mines. They found that seismic tomography can map high stress or seismic active zones during coal extraction, and thereby assess coal burst risks. Moreover, the relationship between displacement, stress and seismicity during mining-induced failure was analysed through a triaxial experiment,[35] numerical modelling approaches,[36,37] and also validated by a large amount of field observations.[38–44] Through these investigations, numerous meaningful qualitative and empirical relationships to understand the link between displacement, stress and seismicity were obtained, which provide a new insight on the mechanism of coal burst processes.

Building upon these empirical relations, different seismic indices for coal burst forecasting have been proposed,[38, 44–48] which includes total seismic energy, number of seismic events, b value, fractal dimension, moment tensor, apparent stress/volume, energy index/ratio, etc. Some of these indices (e.g. total seismic energy, number of seismic events, b value, and fractal dimension) are based on analysing statistical features, the shortcoming of which is that they cannot reflect the dynamic process of coal burst, especially reveal the strain energy transfer in the process of coal burst. Therefore, this kind of statistical indices usually lack understanding of the physical mechanism of coal burst. Due to this limitation, these statistical indices normally provide a qualitative analysis, which can only yield warning notices such 'abnormal seismic values' without the capability of identifying a certain time period or mining area that is susceptible to coal bursts. For the other indices (e.g. energy index/ratio), although with well-defined physical meanings, most of them remain in the level of qualitative trend analysis, which limits the wide dissemination of these indices. Furthermore, many of these indices may even provide contradictory results. For example, as two most commonly applied statistical measures, 'total seismic energy' determined by high and extremely rare high energy events tends to over-estimate the coal burst risk, while on the other hand 'number of seismic events' overwhelmed by a large number of low energy events may under-estimate the risk. This creates another challenge for the application of these indices.

To address the above challenges, this paper presents a seismic-based strain energy methodology by integrating both the seismic energy and the number of seismic events, which reflects the physical process of coal burst and associated strain energy transfer. In the field application, the coal burst process and its associated strain energy transfer during underground coal mining were first investigated using a theoretical approach. Subsequently, the seismic energy derived from the strain energy transfer process was defined and simulated in numerical models. Based on the modelling results, a damage mechanics model was developed to correlate stress, strain, damage and seismic energy release. In this context, a new index named as 'bursting strain energy (BSE)' was proposed to quantitatively assess coal burst propensity. This BSE index was first calibrated via numerical modelling and then successfully applied to a Chinese coal mine for coal burst forecasting.
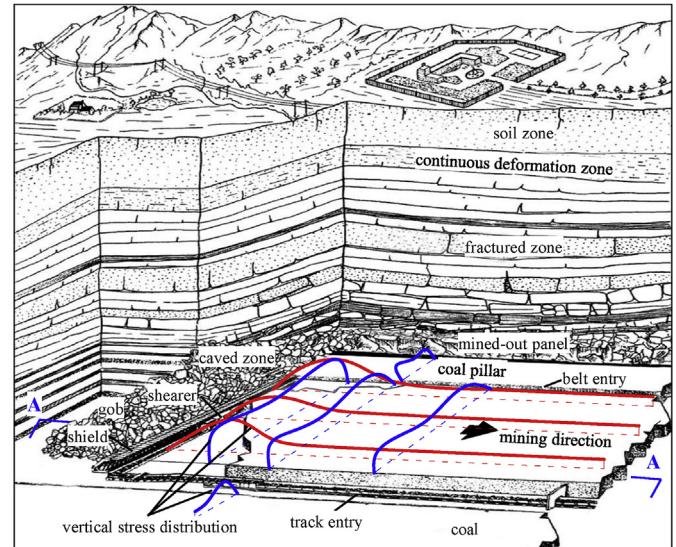

Fig. 1. Three-dimensional view of overburden movement and vertical stress distribution in the coal seam resulting from longwall mining (modified from Peng[49]).

2. Coal burst process and strain energy transfer in underground coal mining

2.1. Underground coal mining and stress redistribution

During underground longwall mining, the removal of solid coal results in the transfer of stress to the front of coal faces and to the side of longwall panels and entries, as shown in Fig. 1. Zones of vertical stress that exceed the in-situ overburden stress are known as abutment zones, and elevated stresses are known as abutment stresses. During mining operation, the abutment stress progresses along with the direction of face advancement, which consequently generates a mostly quasi-static loading on the roof-coal-floor system. Under this quasi-static loading condition, coal fracturing usually starts at the excavation boundary, where the vertical stress is the post-peak residual stress (DE) and transfers gradually to deeper solid coal along with the coal excavation, as shown in Fig. 2. This means that, from deeper solid coal to the excavation boundary, coal gradually experiences the elastic deformation stage (AB), the pre-peak plastic deformation stage (BD) and the post-peak strain softening stage (DE). These three stages often correspond to the zones of continuous, fractured and caved in the overburden strata. In this static loading condition, the strength of coal ($[\sigma]$) (see Fig. 2) increases with the elevated confining stress as the coal locates far away from the excavation boundary. Therefore, abutment stress exceeding coal strength $[\sigma]$ can result in coal failure and release elastic strain energy, which may potentially induce a coal burst.

In addition, the regional stress redistribution as a result of coal extraction may induce far-field fault sliding or roof fracturing and their associated MS events, which in turn may generate an additional dynamic stress applied on the total stresses around the mine opening. This dynamic stress follows an attenuation law ahead of longwall face. In such a case, coal burst is more prone to initiate as long as the total stress, which is the superposition of static stress (i.e. abutment stress) and dynamic stress (i.e. induced by far-field MS events), exceeds the strength of coal in the vicinity of longwall panels and entries.[14–16]

$$\sigma_s + \sigma_d \geq [\sigma] \tag{1}$$

where σ_s is static stress, σ_d is dynamic stress, $[\sigma]$ is the stength of coal.
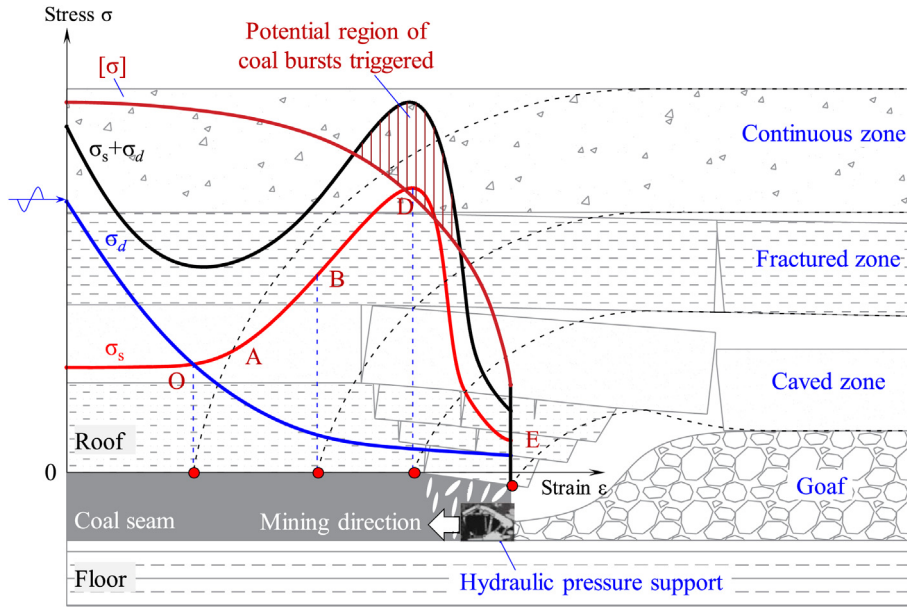
Fig. 2. Overburden movement and zonation as a response to the stress distribution around a mine opening, from section A-A in Fig. 1.

2.2. Coal burst mechanisms and coal failure processes

As shown in Fig. 2, three objects of roof, coal and floor mainly constitute the underground mining space. The interaction of this roof-coal-floor system essentially control coal failure processes and further reveal the coal burst mechanism, which was termed as the double rock sample model or the rigidity theory.[7–9] In this roof-coal-floor system, coal is assumed as a fractured or softened material with non-linear behaviour. The roof and floor are treated as a united surrounding rock system with much larger stiffness and strength than coal. Fig. 3 presents the roof-coal-floor system under static loading condition. The stress behaviour of the surrounding rock under loading is described on the left-hand side. The stress behaviour of coal is displayed on the right-hand side.

It can be inferred from Fig. 3 that, if a tight bonding between coal and surrounding rock was assumed, a strain change ($\Delta\varepsilon_2$) in coal will simultaneously cause surrounding rock (roof and floor) to deform. The strain change ($\Delta\varepsilon_1$) in the surrounding rock can be expressed as:

$$\Delta\varepsilon_1 = \frac{k_2}{k_1}\Delta\varepsilon_2 \tag{2}$$

where k_1 is the stiffness of surrounding rock, k_2 is the stiffness of coal. As

a result, the whole strain ($\Delta\varepsilon$) of the roof-coal-floor system is:

$$\Delta\varepsilon = \Delta\varepsilon_1 + \Delta\varepsilon_2 = \frac{k_1 + k_2}{k_1}\Delta\varepsilon_2 \tag{3}$$

The ratio of coal strain to total strain can be written as:

$$\frac{\Delta\varepsilon_2}{\Delta\varepsilon} = \frac{1}{1 + \frac{k_2}{k_1}} \tag{4}$$

From Eq. (4), the process from stability to instability can be described in the following four stages:

Stage AB: Both k_1 and k_2 are larger than zero. The surrounding rock and coal are both in an elastic energy storage, which is the calm period before coal failure.

Stage BD: The stress-strain curve starts to deviate from the linear section, turns into the inelastic deformation stage and reaches the peak point D. In this stage, k_2 gradually decreases to zero at the peak point and k_1 remains unchanged. Therefore, the surrounding rock is still accumulating elastic strain energy and while coal starts converting elastic energy into plastic deformation. However, the ratio of coal strain to total strain ($\Delta\varepsilon_2/\Delta\varepsilon$) tends to increase as k_2/k_1 decreases. The essence of this change is that the micro-cracks initiated inside the coal start to
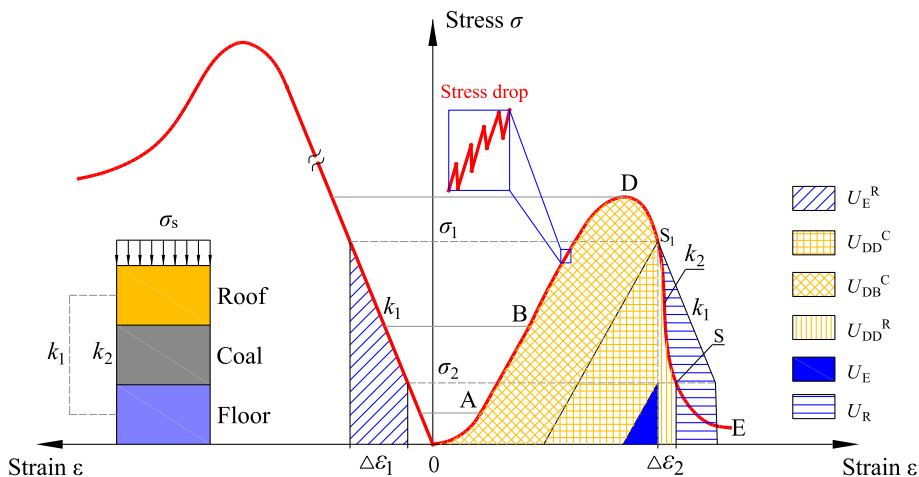

Fig. 3. Energy transfer in roof-coal-floor system during the coal failure process under static loading condition.

grow and extend, which is often accompanied with a sequence of MS events or mild stress drops. This stage corresponds to the pre-failure period.

Stage DS: The stress in coal decreases as it gradually loses its bearing capacity and k_2 turns into a negative value. In this stage, the roof-coal-floor system can reach to an extreme unstable state, i.e., $\Delta\varepsilon_2/\Delta\varepsilon \to \infty$ when $k_1 + k_2 = 0$. At this moment, a dynamic failure event will be triggered, which corresponds to coal burst occurrence.

Stage SE: The failure process in coal gradually slows down and the whole system tends to reach a new stable state. In this stage, $\Delta\varepsilon_2/\Delta\varepsilon$ decreases as k_2 increases again but still less than 0, which corresponds to the calm period after coal burst.

2.3. Strain energy transfer with the additional energy input excluded

In this section, it is assumed that the additional energy input from the external loading stresses (σ_s and σ_d) to facilitate the coal failure process is excluded. In other words, the external loading supply is cut off and as a result the strain energy released from the surrounding rock is the only supply to drive the coal failure process.

According to the energy balance principle, the absorbed energy (U_A) of coal during the failure process contains elastic strain energy (U_E), dissipated energy (U_D) and radiated energy (U_R). This relation can be illustrated in Fig. 3 and expressed as follows:

$$U_A = U_E + U_D + U_R \tag{5}$$

$$U_D = U_{DB}^C + U_{DD}^C + U_{DD}^R \tag{6}$$

$$U_R = U_E^R - U_{DD}^R \tag{7}$$

where U_E is equal to the residual elastic energy in coal after the coal burst. U_E^R is the released elastic energy from the surrounding rock during the coal burst. U_{DB}^C is the energy dissipated by coal before the coal burst. U_{DD}^C is the energy dissipated from the elastic energy storage of coal itself during the coal burst. U_{DD}^R is the energy dissipated from the released elastic energy of the surrounding rock during the coal burst. U_R is equal to the energy released from the roof-coal-floor system during the coal burst, which can be approximated into:

$$U_R = -\frac{k_1 + k_2}{2k_1} \cdot (\sigma_1 + \sigma_2) \cdot \Delta\varepsilon_2 = -\frac{k_1 + k_2}{2k_1 \cdot k_2} \cdot (\sigma_1^2 - \sigma_2^2) \tag{8}$$

where σ_1 and σ_2 are stresses before and after the coal burst, respectively. It can be inferred that when $k_1 + k_2 < 0, U_{SE} > 0$, which agrees well with the unstable coal failure under the loading condition of $k_1 < -k_2$. On the other hand, the stable coal failure under the loading condition of $k_1 \geq -k_2$ corresponds to the case $U_{SE} \leq 0$. For more details about the loading conditions of stable and unstable coal failure, please refer to the reference 6.

2.4. Strain energy transfer without the additional energy input excluded

In this section, the additional energy input from the external loading stresses (σ_s and σ_d) to facilitate the coal failure process is not excluded. In other words, the external input energy is still supplied to accelerate coal deformation and therefore the failure process is normally unstable.

When the roof-coal-floor system is subjected to the external static loading stress (σ_s), an additional input energy ΔU_R needs to be considered, as shown in Fig. 4. As a result, the coal failure process will be violent compared to the loading condition with the additional energy input excluded. In other words, this external loading could be equivalent to the condition that the stiffness of the surrounding rock decreases from k_1 to k_1'. In this context, the position (from S_1 to S_2) where satisfies the condition $k_1 + k_2 = 0$ will be closer to the peak point D and therefore the roof-coal-floor system will reach to the extreme unstable state ($\Delta\varepsilon_2/\Delta\varepsilon \to \infty$) (or initiate the coal burst) earlier.

When the roof-coal-floor system is subjected to the superposition of external static and dynamic loading stresses (σ_s and σ_d), the additional input energy ΔU_R will be larger and the coal failure process will be more violent. As a result, the equivalent decrease of the stiffness of the surrounding rock will be more remarkable. More seriously, the dynamic stress, i.e. cyclic seismic wave loading, is considered as a cyclic loading and unloading with permanent deformation, which may induce the same dynamic failure as the stress reaches the point S_2 even if the stress under static loading condition just reaches the point S_2'.

In conclusion, the coal burst process will be more violent under the superposition condition of static and dynamic loading. This condition is also inclined to initiate coal burst event even in the pre-peak stress state, which is consistent with the potential region of coal burst occurrence displayed in Fig. 2.

3. Stress inversion based on seismic energy

3.1. Definition of seismic energy

As described in Section 2.4, the energy released ($U_R + \Delta U_R$) from the roof-coal-floor system during the coal burst is primarily emitted in the forms of seismic energy, thermal energy and electromagnetic radiation energy. Among these energies, seismic energy can be easily captured and located and thereby widely adopted to measure the intensity of coal burst. Most of researches even considered coal bursts as MS events directly.[38,39,50] By assuming that the amount of energy released during coal failure process will completely convert into seismic waves, the recorded energy (U_{SE}) of MS event can be approximated into the released energy ($U_R + \Delta U_R$).

As described in Section 2.2, the non-linear stage BD is essentially comprised of a sequence of mild stress drops. In this condition, the strain energy transfer process method (Figs. 3 and 4) used for the coal failure process can be also applicable to these multiple stress drops, as shown in Fig. 5. Therefore, for each stress drop, there will be an MS event associated and its energy can be approximated as the released energy ($U_R + \Delta U_R$) as well. But in fact, it is difficult to use the laboratory or the field experimental approach to separate the additional energy input, so that the released energy can hardly be calculated. Numerical experiment approach provides a solution to this problem.

In numerical modelling, Eq. (5) was incorporated into FLAC^{3D} via FISH language to simulate seismic events created during the coal failure process. The absorbed energy in the numerical model was defined as[51]:

$$U_A = \sum_{w=1}^{W} \sum_{n=1}^{N} \left\{ \frac{1}{2} \cdot (\sigma_{ij}^{n,\ w-1} + \sigma_{ij}^{n,\ w}) \cdot \varepsilon_{ij}^{n,w} \cdot V^n \cdot t \right\} \tag{9}$$

where $\sigma_{ij}^{n,\ w}$ and $\varepsilon_{ij}^{n,w}$ are the stress level and strain rate of the element, where the superscript n is the element ID number and w is the current calculation step. t is the time interval between two solution steps. V is the element volume. Subsequently, the embedded functions z_wetot and z_wptot in FLAC^{3D} were used to compute the elastic strain energy (U_E) and dissipated energy (U_D), respectively. Finally, the strain energy released in the next solution step is considered as the seismic energy (U_{SE}) and it can be defined as:

$$U_{SE} = U_R = \sum_{n=1}^{N} (U_A^n - U_E^n - U_D^n) \tag{10}$$

where $U_A^n - U_E^n - U_D^n > 0$.

3.2. Definition of inversed stress using seismic energy and damage variable

According to the continuous damage mechanics,[52] the stress of coal under loading can be elaborated by:

$$\sigma = E\varepsilon(1 - D) \tag{11}$$

where σ is stress, ε is strain, E is Young's modulus, and D is damage variable.
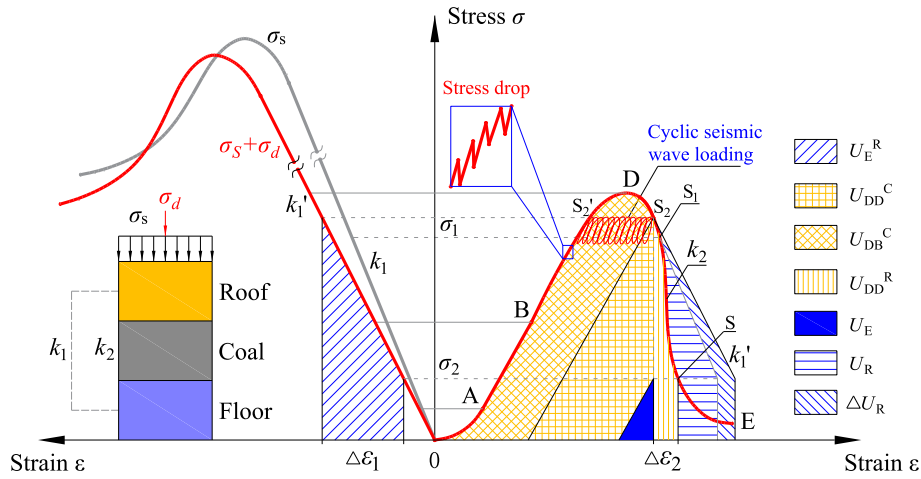
Fig. 4. Energy transfer in roof-coal-floor system during coal failure process under the superposition condition of static and dynamic loading.

To define the damage variable, a number of researchers have adopted the whole strain,[8] plastic strain,[53,54] dissipated energy[55] and seismic source parameters.[56] The former three methods are usually applicable in the analytical modelling, while the last one can be applied on site directly using the field MS monitoring data. In this paper, the Benioff[57] strain derived from seismic energy was utilised to define the damage variable:

$$D = 1 - exp\left(-\frac{\varepsilon_E}{\varepsilon_F}\right) \tag{12}$$

where $\varepsilon_E = \sum \sqrt{U_{SE}}$ is the accumulated Benioff strain. ε_F is the average value of ε_E, which can be determined by assuming that the critical damage $D_F = 0.95$ corresponds to the completely damage state (CDS) (as the point E displayed in Fig. 4) where the ε_E was deemed as the critical Benioff strain (CBS) ε_{EF}. Therefore, ε_F can be calculated by substituting D_F and ε_{EF} into Eq. (12):

$$\varepsilon_F = -\frac{\varepsilon_{EF}}{ln(1 - D_F)} \tag{13}$$

By substituting Eq. (13) into Eq. (11), the inversed stress can be obtained:

$$\sigma_I = E\varepsilon \cdot exp\left(-\frac{\varepsilon_E}{\varepsilon_F}\right) \tag{14}$$

3.3. Numerical simulation of seismic energy, damage, and inversed stress

Above-mentioned procedures were incorporated into the plastic strain-based damage constitute model with its modelling set up parameters proposed in a previous study[53] to simulate the seismic events, and in turn to inverse the stress based on the simulated seismic energy, as shown in Fig. 6.

It can be seen from Fig. 6 (a) and (c) that almost no seismic events generated during the stage AB, which corresponds to the elastic deformation stage. After reaching at the point B, a large number of small micro-cracks are initiated, which results in many small seismic events occurred at the beginning and then to be stable until the point C. This stage BC corresponds to the stable micro-crack growth and extension stage of plastic deformation. During the stage CD, the number of seismic events increases significantly and their amplitudes fluctuate remarkably to release a large amount of energy, which presents the unstable crack extension stage of plastic deformation. In the post-failure stage DE, the coal becomes broken and completely lose bearing capacity at the point E. In this stage, the dynamic failure event corresponding to coal burst occurrence is triggered. The common trends of these stress and seismic evolutions during the failure process of coal can be observed regardless of that under uniaxial loading condition (Fig. 6 (a)) or triaxial loading condition with the confining stress of 1.0 MPa (Fig. 6 (c)), except for that the stress and seismic energy under the triaxial loading condition will be larger than that of uniaxial loading condition, as well as the elastic deformation stage will be longer.
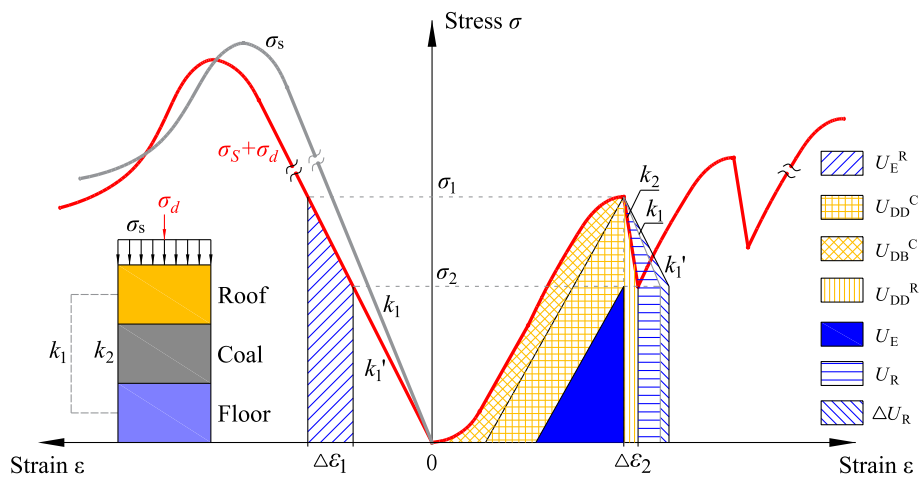

Fig. 5. Energy transfer in roof-coal-floor system during stress drop under the superposition condition of static and dynamic loading.
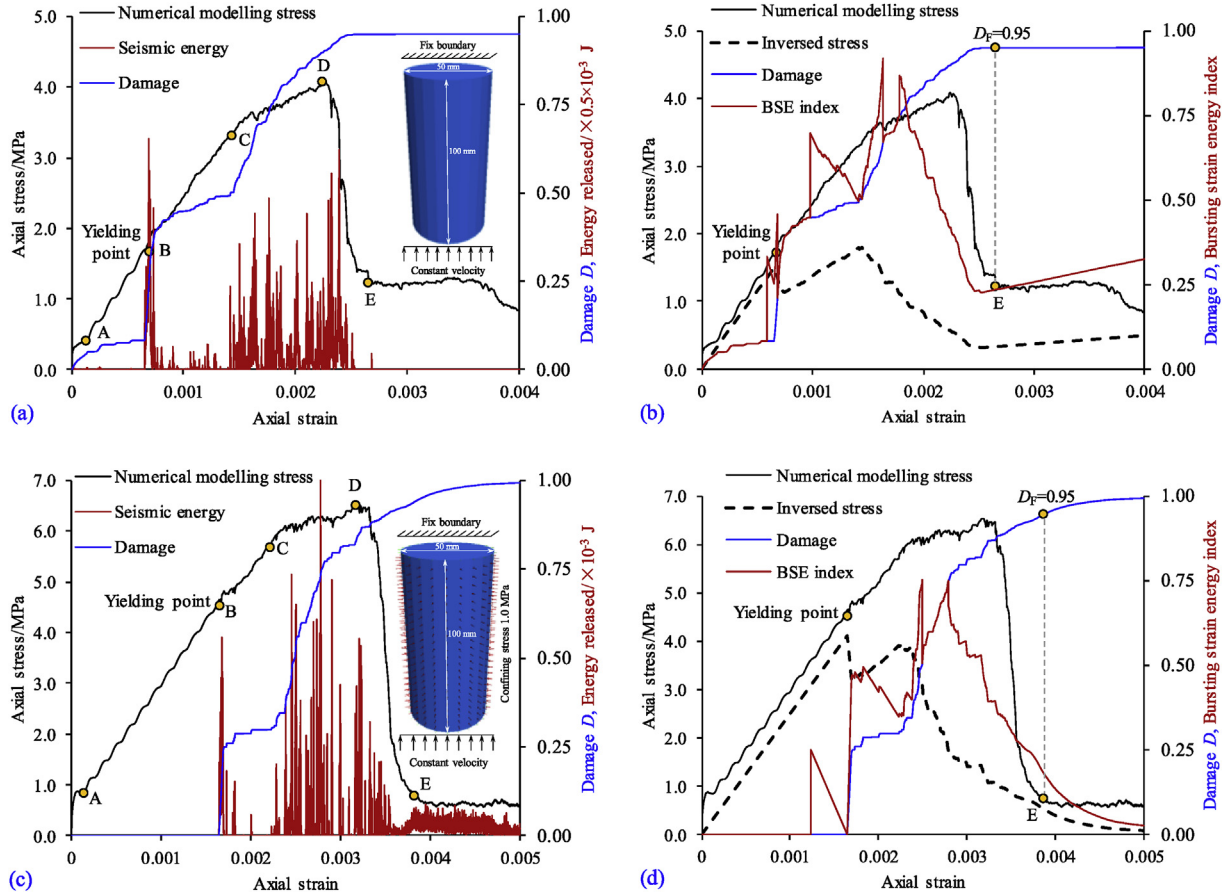
Fig. 6. Seismic energy simulation and the associated inversed stress, damage and bursting strain energy (BSE) index (to be clearly described later in Section 4.1). Seismic and stress evolutions under (a) uniaxial and (c) triaxial loading condition. The evolution of inversed stress, damage and BSE under (b) uniaxial and (d) triaxial loading condition.

Table 1
Relationship between BSE index values range, coal burst risk levels and corresponding guidelines on coal burst control measures (after Dou et al.[58]).

BSE index values range	Coal burst risk levels	Control measures
$0 \leq BSE < 0.25$	None	All mining operations can be carrying out normally.
$0.25 \leq BSE < 0.50$	Weak	More attention should be focused on monitoring and forecasting of coal burst in the process of mining operations.
$0.50 \leq BSE < 0.75$	Moderate	Stress relief measures should be taken to alleviate and eliminate the coal burst risk in the process of mining operations.
$0.75 \leq BSE < 1$	Strong	Production should be paused, and workers must be evacuated from the risk regions immediately. Further mining operations cannot be restored until the coal burst risk has been eliminated by taking the measures and being guaranteed again with the monitoring results.

4. Bursting strain energy index

4.1. Definition of bursting strain energy index

Fig. 6 (b) and (d) present the evolution of damage and inversed stress, where a consistence between the trends of numerical modelling stress and inversed stress is observed, even though there exist large differences in magnitude between them. To forecast the subsequent dynamic failure event, however, the magnitude is not important but the trend will be more interested. In addition, it is believed that the coal failure will be more likely to occur when it reaches a high damage level or a high stress state. But in fact (see Fig. 6), the damage value during stage BD is normally not large but the dynamic failure event is approaching and also the stress might reach to the peak state. In the post-peak stage, the damage value still remain at the high level but the dynamic failure event has been ending and also the stress is decreasing.

To address these issues, a new index was defined:

$$\text{BSE} = \begin{cases} 1 - \left| D - \frac{\sigma_I}{\sigma_p} \right|, & \text{if } D \geq 0.75 \text{ or } \frac{\sigma_I}{\sigma_p} \geq 0.75 \\ D, & \text{if } D < 0.75 \text{ and } \frac{\sigma_I}{\sigma_p} < 0.75 \end{cases}$$

(15)

where $0 \leq BSE \leq 1$, σ_p is the peak of inversed stress. Since this index is deduced from using seismic strain energy and applied for the forecasting of coal bursts, the terminology 'bursting strain energy (BSE)' has been conceived in this paper. Fig. 6 (b) and (d) present the BSE index results in numerical modelling, which indicate that this BSE index could be equally divided into four forecasting levels (none, weak, moderate, and strong) based on the index values ranging from 0 to 0.25, 0.25 to 0.50, 0.50 to 0.75, and 0.75 to 1, respectively, as summarised in Table 1. Under these four different levels, the different control measures of coal burst can be recommended as a guidance accordingly. In addition, these four levels also roughly correspond to the elastic (AB) and completely damage (after E) stage, the plastic stage BC, the parts of plastic stage BC and CD, and the parts of plastic stage CD and post-peak stage DE, respectively.

4.2. Implementation in temporal domain

In field implementation, it should be noted that the strain (ε) in Eq. (14) can hardly be measured for the whole longwall panel directly. But fortunately, it has been known that the loading strain applied on the solid coal ahead of longwall face is approximately proportional to the face advance rate, and the daily MS event number is moderately correlated with the face advance rate.[28,38,42] Therefore, the relation $\varepsilon = \alpha \cdot N_{MS}$ could be assumed into Eq. (14), and the inversed stress can be estimated as:

$$\sigma_I = E \cdot \alpha \cdot N_{MS} \cdot exp\left(-\frac{\varepsilon_E}{\varepsilon_F}\right) \tag{16}$$

where α is the correlation coefficient between strain and seismicity. N_{MS} is the accumulated number of MS events.

Moreover, it can be concluded from Eqs. (12)–(16) that ε_F is a key parameter, and to obtain this value, the completely damage state (CDS) and its correlated critical Benioff strain (CBS) ε_{EF} need to be confirmed first for field implementation. As discussed in Section 2.2, the CDS corresponds to the calm period after coal burst in temporal domain, which is very close to the dynamic failure event. This dynamic failure event is most likely to generate a strong seismic event (also called mainshock) and even trigger a coal burst incident. Therefore, to identify the mainshock in the field implementation is the key step to recognise the CDS.

To achieve this, mainshocks were defined as a set of seismic events whose energy are larger than the critical mainshock energy (CME). This CME can be determined by a linear correlation coefficient method proposed by Cai et al.,[20] as illustrated in Fig. 7. In this figure, the Gutenberg-Richter magnitude-frequency distribution[46] is always skewed in the magnitude of seismic events larger than a threshold value.[27] This threshold value is deemed as the CME. It should be mentioned that this CME is also considered as the region-characteristic maximum possible event magnitude or the upper limit of event magnitude for a given region.[50,59]

It is well known in seismology that foreshocks and/or aftershocks will be recorded around the mainshock, and most of them in magnitude are even approximate to the mainshock. In this context, there should be only one mainshock (maximum energy event) in the above-defined set of mainshocks during a short period, and others should be regarded as foreshocks and/or aftershocks. Therefore, the interval time between any two adjacent strong events (whose energies are larger than the CME) should be also considered to determine the CDS. In other words,
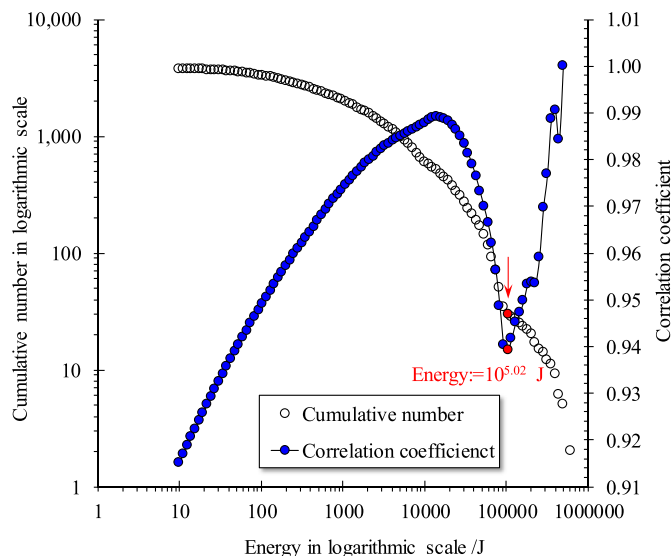
the CDS would be recognised when a seismic event within energy larger than CME occurs, and simultaneously any other events within the same energy level no longer happen in a following certain short period.

In terms of field implementation, the accumulated Benioff strain (ε_E) and the accumulated number of MS events (N_{MS}) in Eqs. (12) and (16) would be reset to zero as long as the CDS has been recognised. It can be realised that there will be several CDSs recognised, so that several CBSs between any two adjacent CDSs will be obtained in the historical seismic sequence as well. In this paper, the median of the CBSs sequence was considered as ε_{EF} further to calculate ε_F using Eq. (13).

4.3. Implementation in spatial domain

As depicted in Fig. 2, the coal along the face advance direction is actually at different stages of the completed stress-strain curve (Fig. 3). This means that when coal at the excavation boundary (at the point E) reaches CDS, the deeper solid coal (at the point A) may just initiate loading condition. When the longwall panel of sufficient width and length is excavated and all MS events are recorded, the maximum value of ε_E will occur around the excavation boundary or even in the gob. This maximum ε_E is considered as ε_{EF} for a given region, and thereby the ε_F can be calculated using Eq. (13) in spatial domain.

In terms of field implementation, the study area is first discretised into small 2D grids or 3D voxels and then the accumulated Benioff strain (ε_E) and the accumulated number of MS events (N_{MS}) are calculated within each grid or voxel. Subsequently, the maximum ε_E is extracted to calculate ε_F, which in turn is feedback to Eqs. (12) and (16) for computing the grid data of damage variable and inversed stress, respectively. Together with the normalisation of inversed stresses, the BSE index values are calculated for each grid or voxel using Eq. (15) and the contour map is plotted using the pixel interpolation accordingly.

4.4. Guidelines on the implementation

Fig. 8 shows the process required to calculate the BSE index in temporal and spatial domains. In the temporal domain, the MS parameters (t and U_{SE}) are used. First, the CME illustrated in Fig. 7 needs to be calculated, which is then utilised to identify the CDSs. On the basis of the CDSs, the CBSs between any two adjacent CDSs are computed and therefore the ε_{EF} is obtained. Subsequently, the ε_F is calculated by substituting ε_{EF} and $D_F = 0.95$ into Eq. (13). Building upon these parameters (ε_F and CDSs) abovementioned and inputting E and α, the BSE index in temporal domain can be calculated using Eqs. (12), (15) and (16).

In the spatial domain, the MS parameters (x, y, z and U_{SE}) are used. First, the ε_E is calculated for each grid, which is then used to identify the CDSs where the ε_E is maximum. This maximum ε_E is deemed as ε_{EF}, and on this basis the ε_F is obtained using Eq. (13). Building upon the parameter (ε_F) and inputting E and α, the BSE index in spatial domain can be calculated using Eqs. (12), (15) and (16).

5. Field application

The Hujiahe coal mine, owned and operated by Shaanxi Binchang Coal Group Company, is located in the west of Shaanxin province, China. The panel of LW 402103 is fairly deep at about 650 m underground deep. The length and width of the panel are approximately 1897 m and 180 m, respectively. The coal seam thickness ranges from 13.00 m to 22.50 m with a maximum dip angle of 9°. The seam is overlain successively by 5.95 m thick sandy mudstone, 23.70 m thick siltstone, and successively underlain by 4.65 m thick mudstone and 4.80 m thick siltstone, as described in Fig. 9. The fully-mechanized top coal caving method was used to recover the panel. The MS monitoring system "ARAMIS M/E" developed by the EMAG of Poland was installed at the mine since September 2013. Fig. 10 depicts the panel geometry
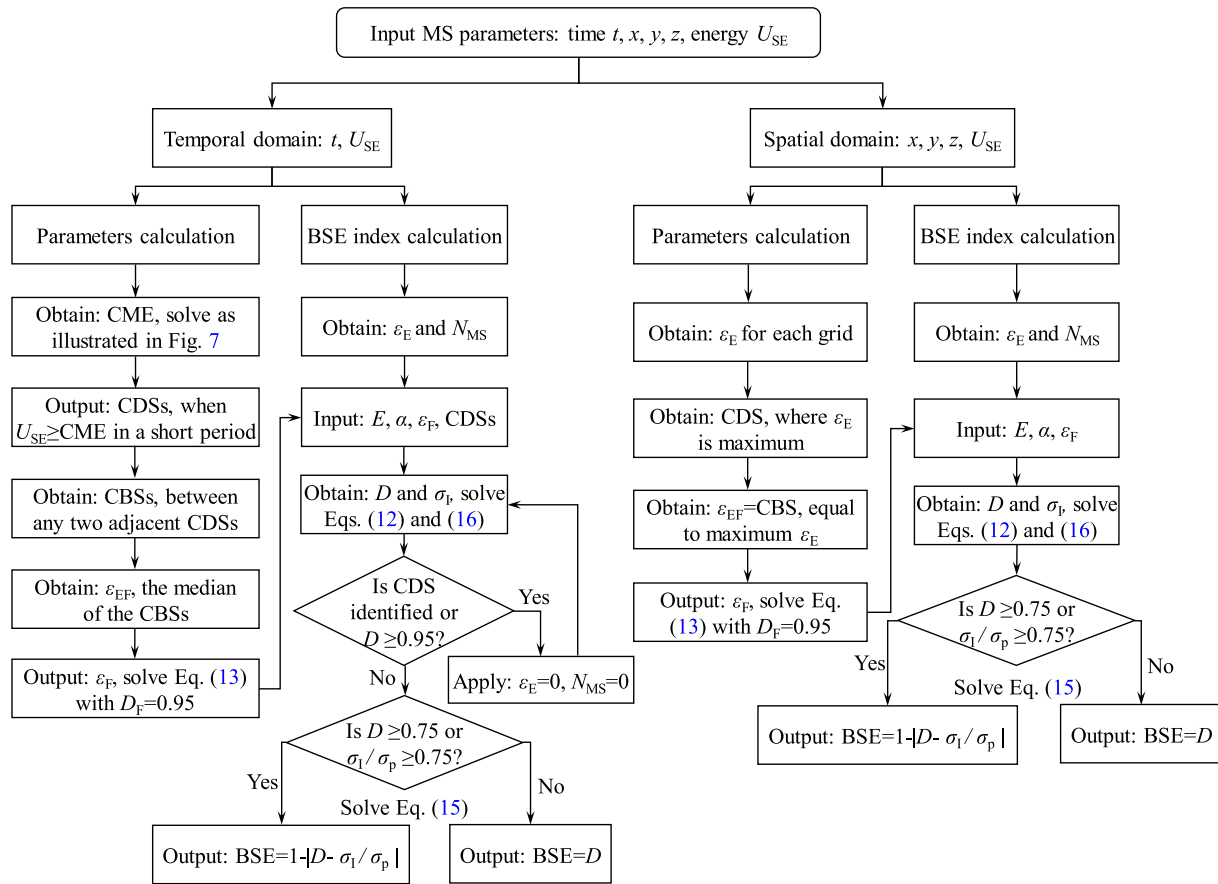

Fig. 7. Calculation of the critical mainshock energy (CME).

Input MS parameters: time t, x, y, z, energy U_{SE}

Temporal domain: t, U_{SE}

- Parameters calculation
  - Obtain: CME, solve as illustrated in Fig. 7
  - Output: CDSs, when $U_{SE} \geq$ CME in a short period
  - Obtain: CBSs, between any two adjacent CDSs
  - Obtain: ε_{EF}, the median of the CBSs
  - Output: ε_F, solve Eq. (13) with D_F=0.95
- BSE index calculation
  - Obtain: ε_E and N_{MS}
  - Input: E, α, ε_F, CDSs
  - Obtain: D and σ_I, solve Eqs. (12) and (16)
  - Is CDS identified or $D \geq 0.95$? — Yes → Apply: ε_E=0, N_{MS}=0
  - No → Is $D \geq 0.75$ or $\sigma_I / \sigma_p \geq 0.75$? Solve Eq. (15)
    - Yes → Output: BSE=1-|D- σ_I / σ_p|
    - No → Output: BSE=D

Spatial domain: x, y, z, U_{SE}

- Parameters calculation
  - Obtain: ε_E for each grid
  - Obtain: CDS, where ε_E is maximum
  - Obtain: ε_{EF}=CBS, equal to maximum ε_E
  - Output: ε_F, solve Eq. (13) with D_F=0.95
- BSE index calculation
  - Obtain: ε_E and N_{MS}
  - Input: E, α, ε_F
  - Obtain: D and σ_I, solve Eqs. (12) and (16)
  - Is $D \geq 0.75$ or $\sigma_I / \sigma_p \geq 0.75$? Solve Eq. (15)
    - Yes → Output: BSE=1-|D- σ_I / σ_p|
    - No → Output: BSE=D

Fig. 8. Flowchart for the calculation of bursting strain energy (BSE) index in temporal and spatial domains.

Lithology	Depth(m)	Thickness(m)	Geology columnar
Sandy mudstone and siltstone	561.27	52.13	
Fine mudstone	568.75	7.30	
Sandy mudstone	592.90	24.15	
Medium sandstone	603.10	10.20	
Siltstone	626.80	23.70	
Sandy mudstone	632.75	5.95	
Coal	658.55	22.50	
Mudstone	663.20	4.65	
Siltstone	668.00	4.80	

Fig. 9. General stratigraphy of the LW 402103 panel in Hujiahe coal mine.

and seismic stations that installed in the research area. For further details of this monitoring system used, please refer to the reference 44.

A destructive coal burst event stuck the mine at 22:21 pm on October 27, 2016 (local time). According to the MS monitoring results, this coal burst was caused by a large seismic event with 2.76×10^5 J of energy release at the rib of belt entry and its hypocentre was located in the roof, 7 m in front of the longwall face and 25 m away from the belt entry (Fig. 10). This event was even felt at the mine ground office building. Damages in the field are described as follows: within 15 m radius of burst areas at the belt entry, the roof and entry sides were cut off and sunk by 600 mm-1000 mm, demonstrated as the burst area R1 in Fig. 10. The floor in burst area R2 of the drainage entry heaved for 200 mm and cracked for 40 mm in width. Moreover, the cross section of the entry was seriously deformed.

In order to acquire the critical parameters for the calculation of BSE index in temporal domain, all the MS events recorded over last six months were collected. Using the calculation method described in Section 4.2, the value of the CME is computed as $10^{5.02}$ J (see Fig. 7) and ε_F is 11242 J$^{1/2}$. The Young's modulus (E = 870 MPa) of the coal and the coefficient (see Eq. (16), α = 0.00072 in temporal domain) between strain and seismicity were adopted in this paper. Note that the parameters (E and α) will not change the shape of stress curve, and therefore will not change the final BSE index results. In field implementation, they are only utilised to adjust the stress scale. Fig. 11 presents the results of the inversed stress, damage variable and BSE index. It can be seen that all mainshocks (including foreshocks and/or aftershocks) occurred after the peak stress. Most of them even occurred in the strong risk level with the BSE index value larger than 0.75. In particular, prior to the coal burst occurred at October 27, 2016, the BSE index reached to a strong level in the early time of October 25 and maintained at the strong level (BSE ≥ 0.75) until the coal burst
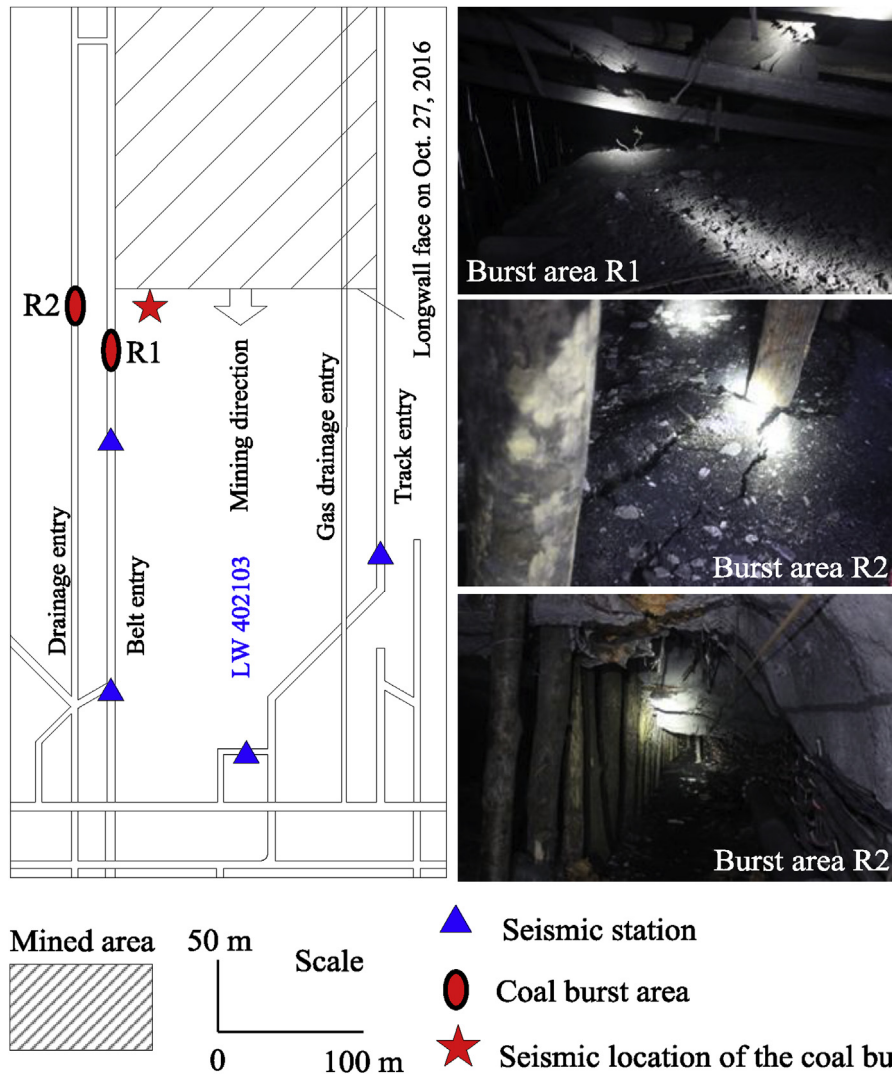
Fig. 10. Layout of LW 402103 panel and seismic stations installed in the research area, and the location and destroyed zones of the coal burst event occurred at 22:21 pm on October 27, 2016.
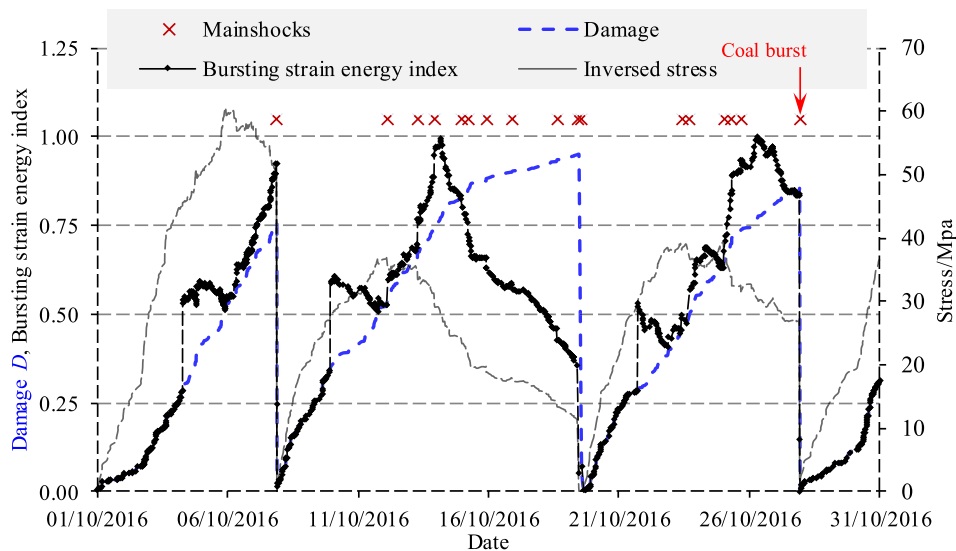

Fig. 11. The evolution of the inversed stress, damage variable and bursting strain energy (BSE) index.
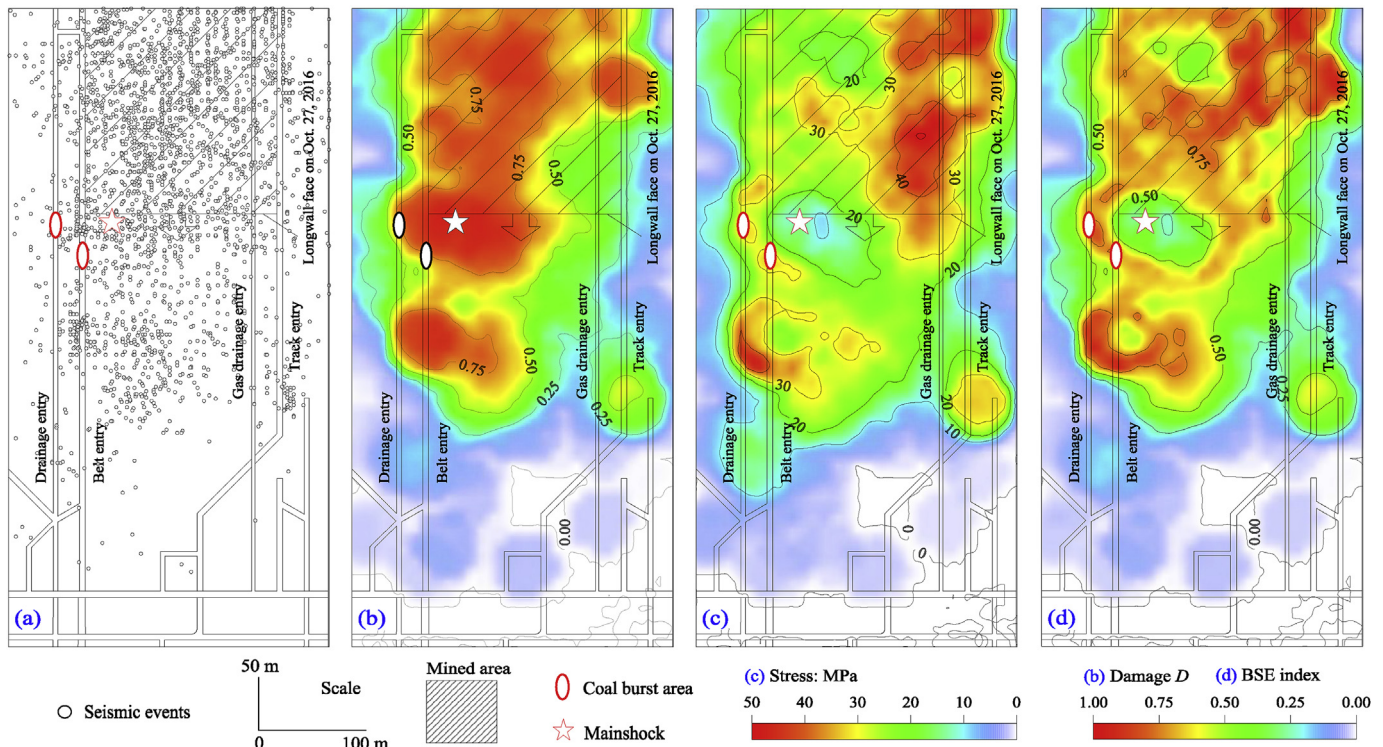
Fig. 12. Plan views of (a) the spatial distribution of seismic events (from 1 May to 26 October 2016), (b) Damage variable *D*, (c) inversed stress, and (d) bursting strain energy (BSE) index prior to the coal burst event occurred on October 27, 2016.

occurred.

With respect to the calculation of the BSE index in spatial domain, the monitoring region was first discretised into 2D small grids of 10 m × 10 m. The accumulated Benioff strain (ε_E) and the accumulated number of MS events (N_{MS}) were then calculated within each grid using the same set of recorded MS data from 1 May to 26 October 2016, as displayed in Fig. 12(a). Subsequently, the maximum ε_E was assigned to be ε_{EF}, and thus the ε_F was calculated using Eq. (13). This ε_F in turn was feedback to Eq. (12) to compute the damage variable (Fig. 12(b)). The inversed stress (Fig. 12(c)) was then calculated using Eq. (16), together with setting the Young's modulus (*E* = 870 MPa) of the coal and the coefficient (see Eq. (16), α = 0.001 in spatial domain) between strain and seismicity. Finally, the BSE index values were calculated using Eq. (15) and the contour maps were plotted in Fig. 12(d) via the pixel interpolation accordingly. It can be seen that the seismic location of the coal burst was identified in the high damage zone, which corresponds to the low stress region and the low value region of the BSE index. It might be the reason that the coal in this high damage state had lost its bearing capacity, which would result in a high likelihood of roof subsidence and therefore induce the strong seismic event located in the roof. The destroyed zones (burst areas R1 and R2) were located in the vicinity of the high damage region as demonstrated by the damage variable *D* = 0.75, which corresponds to the relatively high stress (larger than 30 MPa) region and the strong risk region of BSE ($\geq$0.75) index. Note that more attention should be taken when regions highlighted above are near the entries and around the longwall face, other than that in the deeper solid coal or even in the gob far away. It is because the entries would be more likely to be destroyed by the coal burst event while the strong risk regions indicated around these entries are closer to the longwall face.

6. Conclusions

In this paper, a new seismic-based strain energy methodology was developed for the quantitative analysis of coal burst forecasting, which

reflects the physical process of coal burst and associated strain energy transfer in underground coal mining. Three main conclusions are drawn as follows:

The theoretical analysis of the strain energy transfer in the process of coal burst during underground coal mining revealed that the coal burst process is a result of the strain energy released from the surrounding rock, plus the additional energy input from the superposition of static and dynamic stresses.

The seismic energy, derived from the strain energy transfer process, was defined and simulated in numerical models. With the modelling results, a damage mechanics model was developed to correlate the stress, strain, damage and seismic energy. On this basis, a new index was defined in a quantitative form named as 'bursting strain energy (BSE)' and simultaneously calibrated in the numerical modelling.

In the field implementation, the BSE index was defined in temporal and spatial domains accordingly using the seismic energy and the number of seismic events. The application of the BSE index has been successfully demonstrated at a coal mine in China for the coal burst forecasting using MS monitoring data. Results showed that the BSE index can effectively indicate the likelihood of coal burst occurrence in temporal domain and assess the high risk region in spatial domain. Such application can be conducted on a daily basis within the real-time MS monitoring data, which can help improve mining safety and productivity.

References

1. Cook NGW. A note on rockbursts considered as a problem of stability. *J S Afr Inst Min Metall.* 1965;65(8):437–446.
2. Bräuner G. *Rockbursts in Coal Mines and Their Prevention.* AA Balkema Rotterdam; 1994.
3. Romashov AN, Tsygankov SS. Generalized model of rock bursts. *J Min Sci.* 1993;28(5):420–423.
4. Hudson JA, Crouch SL, Fairhurst C. Soft, stiff and servo-controlled testing machines: a review with reference to rock failure. *Eng Geol.* 1972;6(3):155–189.
5. Singh SP. Burst energy release index. *Rock Mech Rock Eng.* 1988;21(2):149–155.
6. Xu YH, Cai M. Influence of strain energy released from a test machine on rock failure process. *Can Geotech J.* 2017;55(6):777–791.
7. Salamon MDG. Stability, instability and design of pillar workings. *Int J Rock Mech Min Sci Geomech Abstr.* 1970;7(6):613–631.
8. Chen ZH, Tang CA, Huang RQ. A double rock sample model for rockbursts. *Int J Rock Mech Min Sci.* 1997;34(6):991–1000.
9. Ma TH, Tang CA, Tang SB, et al. Rockburst mechanism and prediction based on microseismic monitoring. *Int J Rock Mech Min Sci.* 2018;110:177–188.
10. Linkov AM. Rockbursts and the instability of rock masses. *Int J Rock Mech Min Sci Geomech Abstr.* 1996;33(7):727–732.
11. Kidybinski A. Bursting liability indices of coal. *Int J Rock Mech Min Sci Geomech Abstr.* 1980;17:167–171.
12. Wang JA, Park HD. Comprehensive prediction of rockburst based on analysis of strain energy in rocks. *Tunn Undergr Space Technol.* 2001;16(1):49–57.
13. Cai W, Dou LM, Si GY, Cao AY, He J, Liu S. A principal component analysis/fuzzy comprehensive evaluation model for coal burst liability assessment. *Int J Rock Mech Min Sci.* 2016;81:62–69.
14. Dou LM, Mu ZL, Li ZL, Cao AY, Gong SY. Research progress of monitoring, forecasting, and prevention of rockburst in underground coal mining in China. *Int J Coal Sci Technol.* 2014;1(3):278–288.
15. He J, Dou LM, Gong SY, Li J, Ma ZQ. Rock burst assessment and prediction by dynamic and static stress analysis based on micro-seismic monitoring. *Int J Rock Mech Min Sci.* 2017;93:46–53.
16. Li ZL, Dou LM, Wang GF, Cai W, He J, Ding YL. Risk evaluation of rock burst through theory of static and dynamic stresses superposition. *J Cent South Univ.* 2015;22(2):676–683.
17. Cao WZ, Shi JQ, Si GY, Durucan S, Korre A. Numerical modelling of microseismicity associated with longwall coal mining. *Int J Coal Geol.* 2018;193:30–45.
18. Tang CA, Wang JM, Zhang JJ. Preliminary engineering application of microseismic monitoring technique to rockburst prediction in tunneling of Jinping II project. *J Rock Mech Geotech Eng.* 2010;2(3):193–208.
19. Si GY, Durucan S, Jamnikar S, et al. Seismic monitoring and analysis of excessive gas emissions in heterogeneous coal seams. *Int J Coal Geol.* 2015;149:41–54.
20. Cai W, Dou LM, Li ZL, Liu J, Gong SY, He J. Microseismic multidimensional information identification and spatio-temporal forecasting of rock burst: a case study of Yima Yuejin coal mine, Henan, China. *Chin J Geophys-Ch.* 2014;57(8):2687–2700.
21. Maxwell SC, Young RP. Seismic imaging of rock mass responses to excavation. *Int J Rock Mech Min Sci Geomech Abstr.* 1996;33(7):713–724.
22. Li XL, Wang EY, Li ZH, Liu ZT, Song DZ, Qiu LM. Rock burst monitoring by integrated microseismic and electromagnetic radiation methods. *Rock Mech Rock Eng.* 2016;49(11):4393–4406.
23. Dou LM, He XQ. *Theory and Technology of Rock Burst Prevention.* Xuzhou: China University of Mining and Technology Press; 2001.
24. Qu XC, Jiang FX, Yu ZX. Rockburst monitoring and precaution technology based on equivalent drilling research and its application. *Chin J Rock Mech Eng.* 2011;30(11):2346–2351.
25. Tan YL, Yu FH, Chen L. A new approach for predicting bedding separation of roof strata in underground coalmines. *Int J Rock Mech Min Sci.* 2013;61:183–188.
26. Alber M, Fritschen R, Bischoff M, Meier T. Rock mechanical investigations of seismic events in a deep longwall coal mine. *Int J Rock Mech Min Sci.* 2009;46(2):408–420.
27. Amitrano D. Variability in the power-law distributions of rupture events. *Eur Phys J Spec Top.* 2012;205:199–215.
28. Si GY. *An Investigation into Gas Emission and Outburst Control in Thick Seam Coal Mining.* Dissertation, Imperial College London; 2015.
29. Friedel MJ, Jackson MJ, Williams EM, Olson MS, Westman E. Tomographic imaging of coal pillar conditions: observations and implications. *Int J Rock Mech Min Sci Geomech Abstr.* 1996;33(3):279–290.
30. Luxbacher K, Westman E, Swanson P, Karfakis M. Three-dimensional time-lapse velocity tomography of an underground longwall panel. *Int J Rock Mech Min Sci.* 2008;45:478–485.
31. Luo X, King A, Van de Werken M. Tomographic imaging of rock conditions ahead of mining using the shearer as a seismic source-a feasibility study. *IEEE T Geosci Remote.* 2009;47:3671–3678.
32. Cai W, Dou LM, Cao AY, Gong SY, Li ZL. Application of seismic velocity tomography in underground coal mines: a case study of Yima mining area, Henan, China. *J Appl Geophys.* 2014;109:140–149.
33. Cai W, Dou LM, Gong SY, Li ZL, Yuan SS. Quantitative analysis of seismic velocity tomography in rock burst hazard assessment. *Nat Hazards.* 2015;75(3):2453–2465.
34. Gong SY, Li J, Ju F, Dou LM, He J, Tian XY. Passive seismic tomography for rockburst risk identification based on adaptive-grid method. *Tunn Undergr Space Technol.* 2019;86:198–208.
35. He MC, Miao JL, Feng JL. Rock burst process of limestone and its acoustic emission characteristics under true-triaxial unloading conditions. *Int J Rock Mech Min Sci.* 2010;47(2):286–298.
36. Snelling PE, Godin L, McKinnon SD. The role of geologic structure and stress in triggering remote seismicity in Creighton Mine, Sudbury, Canada. *Int J Rock Mech Min Sci.* 2013;58:166–179.
37. Zhu WC, Li ZH, Zhu L, Tang CA. Numerical simulation on rockburst of underground opening triggered by dynamic disturbance. *Tunn Undergr Space Technol.* 2010;25(5):587–599.
38. Srinivasan C, Arora SK, Yaji RK. Use of mining and seismological parameters as premonitors of rockbursts. *Int J Rock Mech Min Sci.* 1997;34(6):1001–1008.
39. Ortlepp WD. Observation of mining-induced faults in an intact rock mass at depth. *Int J Rock Mech Min Sci.* 2000;37(1):423–436.
40. Sprenke KF, White BG, Rohay AC, Whyatt JK, Stickney MC. Comparison of body-wave displacement with damage observations of a rockburst, coeur d'Alene mining district, Idaho. *Bull Seismol Soc Am.* 2002;92(8):3321–3328.
41. Driad-Lebeau L, Lahaie F, Al Heib M, Josien JP, Bigarre P, Noirel JF. Seismic and geotechnical investigations following a rockburst in a complex French mining district. *Int J Coal Geol.* 2005;64(1):66–78.
42. Shen B, King A, Guo H. Displacement, stress and seismicity in roadway roofs during mining-induced failure. *Int J Rock Mech Min Sci.* 2008;45(5):672–688.
43. Leśniak A, Isakow Z. Space-time clustering of seismic events and hazard assessment in the Zabrze-Bielszowice coal mine, Poland. *Int J Rock Mech Min Sci.* 2009;46(5):918–928.
44. Cai W, Dou LM, Zhang M, Cao WZ, Shi JQ, Feng LF. A fuzzy comprehensive evaluation methodology for rock burst forecasting using microseismic monitoring. *Tunn Undergr Space Technol.* 2018;80:232–245.
45. Gibowicz SJ, Kijko A. *An Introduction to Mining Seismology.* San Diego: Academic Press; 1994.
46. Gutenberg B, Richter CF. Frequency of earthquakes in California. *Bull Seismol Soc Am.* 1944;34(4):185–188.
47. Mendecki AJ. *Seismic Monitoring in Mines.* Springer Science & Business Media; 1996.
48. Xie HP, Pariseau WG. Fractal character and mechanism of rock bursts. *Int J Rock Mech Min Sci Geomech Abstr.* 1993;30(4):343–350.
49. Peng SS. *Longwall Mining.* second ed. Englewood, USA: Society for Mining, Metallurgy, and Exploration, Inc. (SME); 2006.
50. Kijko A, Singh M. Statistical tools for maximum possible earthquake magnitude estimation. *Acta Geophys.* 2011;59(4):674–700.
51. Wang J, Wang Z, Yang S. A coupled macro-and meso-mechanical model for heterogeneous coal. *Int J Rock Mech Min Sci.* 2017;94:64–81.
52. Lemaitre J. A continuous damage mechanics model for ductile fracture. *J Eng Mater Technol.* 1985;107(1):83–89.
53. Cai W, Dou LM, Ju Y, Cao WZ, Yuan SS, Si GY. A plastic strain-based damage model for heterogeneous coal using cohesion and dilation angle. *Int J Rock Mech Min Sci.* 2018;110:151–160.
54. Yang SQ, Hu B, Xu P. Study on the damage-softening constitutive model of rock and experimental verification. *Acta Mech Sinica-PRC.* 2019 online https://doi.org/10.1007/s10409-018-00833-y.
55. Yang SQ, Xu P, Ranjith PG. Damage model of coal under creep and triaxial compression. *Int J Rock Mech Min Sci.* 2015;100(80):337–345.
56. Zhao Y, Yang T, Zhang P, Zhou J, Yu Q, Deng W. The analysis of rock damage process based on the microseismic monitoring and numerical simulations. *Tunn Undergr Space Technol.* 2017;69:1–17.
57. Benioff H. Earthquakes and rock creep:(Part I: creep characteristics of rocks and the origin of aftershocks). *Bull Seismol Soc Am.* 1951;41(1):31–62.
58. Dou LM, Lu CP, Mu ZL, Gao MS. Prevention and forecasting of rock burst hazards in coal mines. *Min Sci Technol.* 2009;19(5):585–591.
59. Wesseloo J. The spatial assessment of the current seismic hazard state for hard rock underground mines. *Rock Mech Rock Eng.* 2018;51(6):1839–1862.